being no evidence for a twenty-two year period. While the mechanism of solar control is still obscure, we have earlier interpreted the new results as indicative of continuous solar emission of cosmic rays and changes of $M\phi^D$ as caused by magnetic bending of the trajectories of charged solar particles. The consistent world-wide character of changes of $M\phi^D$ is then not surprising.

Coronal emission in 5303 A is the most satisfactory index we know for activity in solar cosmic-ray emission. This is demonstrated strikingly in 1943, and in the pronounced shift of $M\phi^D$ in 1947 to later hours. Therefore, Simpson's observations with neutrons relating to low-energy primaries and the daily variation of mesons related to a more energetic primary component both lead to the same conclusion. They must focus our attention on the solar corona for an understanding of the processes of continuous cosmic-ray emission from the sun.

We are deeply indebted to Dr. S. E. Forbush and to Professor Waldmeier for furnishing the unpublished data, which have made the present study possible. It is a pleasure to acknowledge assistance from Mr. K. A. Gidwani, Mr. Duggal, and Mr. Bhatt, and support from the Atomic Energy Commission of India.

PHYSICAL REVIEW VOLUME 96, NUMBER 2 OCTOBER 15, 1954

Precision Measurement of the Negative Pion Mass from Its Radiative Absorption in Hydrogen*†

KENNETH M. CROWE‡ AND ROBERT H. PHILLIPS§
Radiation Laboratory, Department of Physics, University of California, Berkeley, California
(Received March 9, 1954)

The gamma-ray spectrum of the reaction

$$\pi^- + p \rightarrow n + \gamma$$

has been remeasured with an improved design of the high-energy pair spectrometer. This design has taken advantage of one of the focusing properties of a 90-degree wedge-shaped magnetic field to minimize the effect on the resolving power of multiple scattering of the pair fragments in the converter. The theory of the spectrometer is developed in detail. The accuracy of the energy scale depends on magnetic field measurements and the calculation of orbits, aberrations, and resolving power. By the determination of the mesonic absorption gamma-ray energy, a precise mass value for the negative pion has been found:

$$M_{\pi^-} = 272.7 \pm 0.3 m_e.$$

From the $\pi^- - \pi^0$ mass differences already obtained by Panofsky, Aamodt, and Hadley (PAH), by Chinowsky, Sachs, and Steinberger (CSS), and the $\pi^- - \mu^-$ mass difference obtained by Lederman, Tinlot, and Booth (LTB), it is possible to improve the mass values for the π^0 and the μ^- mesons.

From $\pi^- - \pi^0$ (PAH): $M_{\pi^0} = 262.2 \pm 2.0\ m_e$;
from $\pi^- - \pi^0$ (CSS): $M_{\pi^0} = 263.9 \pm 0.7\ m_e$;
from $\pi^- - \mu^-$ (LTB): $M_{\mu^-} = 206.7 \pm 3.0\ m_e$.

If one assumes that the positive and negative pions have the same mass, the mass of the positive muon can also be deduced from the work of Birnbaum, Smith, and Barkas:

$$M_{\mu^+} = 206.3 \pm 0.3\ m_e.$$

I. INTRODUCTION

MANY experimenters have in the course of studies both with cosmic rays and artificial sources, measured the pion and muon masses and several relations between them to varying accuracy. This group of experiments is summarized in several review articles.[1–3]

To date only one of these experiments, other than the present work, has been carried to an accuracy better than a half percent (~1 electron mass). This experiment was started by the late Dr. Eugene Gardner several years ago, and has been carried on by the nuclear emulsion group at Berkeley[4]; results have appeared at various stages of completion.[5]

Since the mass relations obtained in this manner will

* Presented by K. M. Crowe in partial fulfillment of the degree of Doctor of Philosophy.
† This work was done under the auspices of the U. S. Atomic Energy Commission.
‡ Now at Stanford University, Stanford, California.
§ Now at Brookhaven National Laboratory, Upton, New York.
[1] C. F. Powell, Repts. Progr. Phys. **13**, 350 (1950).
[2] Hugh Bradner, University of California Radiation Laboratory Report No. UCRL-486, 1949 (unpublished).
[3] W. K. H. Panofsky and K. M. Crowe in *Experimental Nuclear Physics*, edited by E. Segrè (John Wiley and Sons, Inc., New York), Vol. III (in preparation).
[4] Smith, Barkas, Bradner, and Gardner, Phys. Rev. **78**, 86 (1950); Bradner, Smith, Barkas, and Bishop, Phys. Rev. **77**, 462 (1950); Barkas, Smith, and Gardner, Phys. Rev. **82**, 102 (1951).
[5] Birnbaum, Smith, and Barkas, Phys. Rev. **83**, 895 (1951); Phys. Rev. **91**, 765 (1953); and W. Birnbaum (to be submitted to Revs. Modern Phys.).

be used to derive the muon mass, we will briefly sketch the methods involved and give their current results.

The basic method of the Gardner mass-measurement technique assumes that one can compare directly the purely electromagnetic interactions of the meson and the proton. This is done by a precise measurement of the ratio of the ranges in the same nuclear emulsions and at the same time measuring the ratio of the momenta as defined by the orbits in the cyclotron magnetic field (Fig. 1).

By choosing the proper orbits it is possible to eliminate from the mass calculation the details of the energy loss relations if one makes the usual assumption that the energy loss depends only on the velocity of the particles.

A comprehensive summary of the theory for this method is described by Barkas.[6] It will suffice to point out that the major source of error appearing in the measurement is statistical and results from the range straggling producing a distribution in the final mass ratio. The results of these measurements are as follows[7]:

$$M_{\pi^+}=273.3\pm0.2\ m_e, \tag{1}$$

$$M_{\pi^-}=272.7\pm0.3\ m_e. \tag{2}$$

An additional experiment which compares positive decay muons with pions permits the accurate evaluation of mass difference. One assumes the decay reaction to be

$$\pi^+\rightarrow\mu^++\nu. \tag{3}$$

The derived $\pi^+-\mu^+$ mass difference depends on the decay momentum and the mass ratio and is found to be[5]

$$M_{\pi^+}-M_{\mu^+}=66.41\pm0.07\ m_e. \tag{4}$$

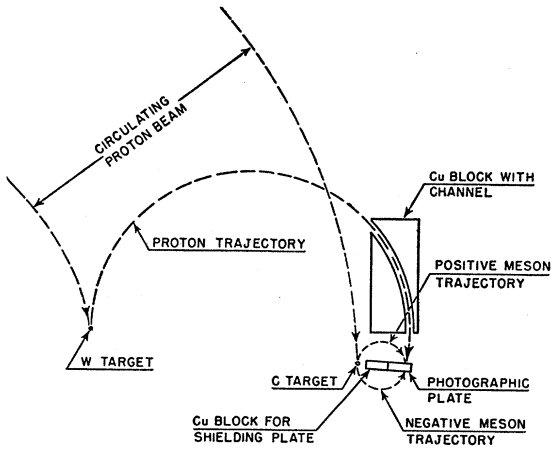

FIG. 1. Diagram illustrating geometry of experiment to measure meson to proton mass ratios by the Gardner technique.

[6] Walter H. Barkas, University of California Radiation Laboratory Report No. UCRL-2327, 1953 (to be submitted to Revs. Modern Phys.); Walter H. Barkas, Am. J. Phys. **20**, 5 (1952).

[7] Frances M. Smith, University of California Radiation Laboratory Report No. UCRL-2371, 1954 (to be submitted to Revs. Modern Phys.).

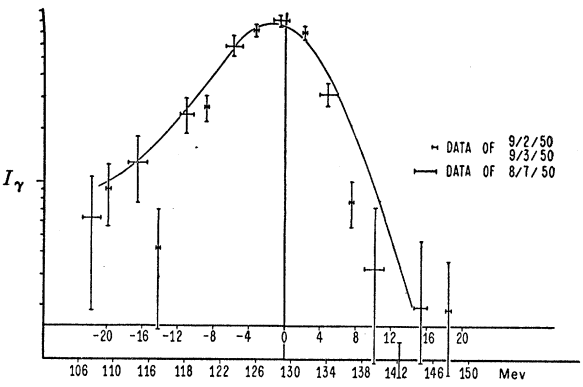

FIG. 2. The gamma-ray energy spectrum with the theoretical resolving power used in previous π^- mass measurements. The resolution does not include ionization loss, converter horizontal width corrections, or energy scale corrections due to fringe field. Probable errors are shown.

The error of this measurement involves the statistical distribution caused by range fluctuations. An absolute field measurement is necessary for calculating the decay momentum and was made with a nuclear induction fluxmeter.

The decay in flight of π^- mesons has been observed in a cloud chamber by Lederman, Tinlot, and Booth.[8] The momenta of the π^- a d μ^- were measured and from the kinematics they obtained a mass difference for negative mesons,

$$M_{\pi^-}-M_{\mu^-}=66.0\pm3.0\ m_e. \tag{5}$$

Since the current measurement of the negative pion mass was an outgrowth of the work of Panofsky *et al.*,[9] we shall also briefly summarize their mass measurement results.

By using a multichannel pair spectrometer, they measured the gamma-ray spectrum which resulted when π^- mesons came to rest in hydrogen gas.

$$\begin{aligned}&\pi^-+p\rightarrow n+\gamma,\\ &\pi^-+p\rightarrow n+\pi^0,\quad \pi^0\rightarrow 2\gamma.\end{aligned} \tag{6}$$

The radiative absorption results in a monochromatic line of energy approximately equal to the rest energy of the pion less the recoil of the neutron. The spectrum they obtained is shown in Fig. 2.

The energy of this gamma ray was evaluated knowing the geometry of the detectors and the magnetic field of the spectrometer, and from this they obtained a mass

$$M_{\pi^-}=275.2\pm2.5\ m_e. \tag{7}$$

In the subsequent analysis of the spectrometer used in the current measurement, several small corrections were made which were omitted in the above mass value, the major one being the ionization loss of the pair frag-

[8] Lederman, Tinlot, and Booth, Phys. Rev. **81**, 281 (1951).

[9] Panofsky, Aamodt, and Hadley, Phys. Rev. **81**, 565 (1951), and private communications; Phys. Rev. **80**, 94, 282 (1950); Panofsky, Aamodt, and York, Phys. Rev. **78**, 89 (1950).

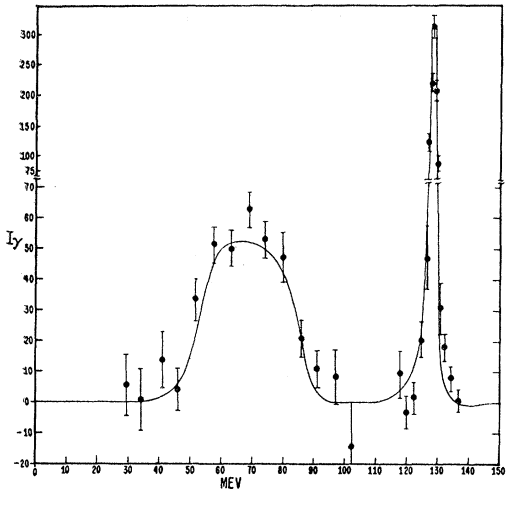

FIG. 3. Composite plot of γ-ray spectrum resulting from the capture of negative pions in hydrogen. Note that the scale of the ordinate is expanded by a factor of five below $I_\gamma=75$ Mev to show details of the π^0 peak.

ments leaving the converter. The corrected value should be $\sim 278\ m_e$. The error of this measurement has not been reanalyzed since there is considerable uncertainty in such an analysis without extensive remeasurements of the magnetic field.

From the branching into π^0 and subsequent Doppler shift of the decay gamma rays, they were able to establish the difference between the masses of the charged and neutral pion,

$$M_{\pi^-}-M_{\pi^0}=10.5\pm 2\ m_e. \tag{8}$$

The error of this measurement results almost entirely from the small number of events as seen from Fig. 3, a composite plot of the previous results and the present radiative capture line. A further improvement in the accuracy of neutral meson mass would be possible by a remeasurement of this π^0 spectrum.

Chinowsky, Sachs, and Steinberger[10] have studied the angular correlation of the gamma rays of the reaction Eq. (6). The aberration of the decay gamma rays caused by the motion of the π^0 has yielded a precise measure of the mass difference,

$$M_{\pi^-}-M_{\pi^0}=8.8\pm 0.6\ m_e. \tag{9}$$

II. THE FOCUSING PAIR SPECTROMETER AND THE EXPERIMENTAL METHOD

The absorption equipment shown in Fig. 4 was the same as that used by Panofsky *et al.*[9] Mesons which are produced at the cyclotron target stop in a vessel (Fig. 5) filled with hydrogen. The resulting gamma-ray spectrum is measured with a pair spectrometer. A background spectrum is measured when the vessel is evacuated, and this is subtracted off.

The improvement in resolution of the spectrometer was accomplished by redesigning the detection array in such a way as to achieve a refocusing in the horizontal plane for particles which have multiply scattered when leaving the converter. The location of the "focus line" was found by a series of orbit calculations.

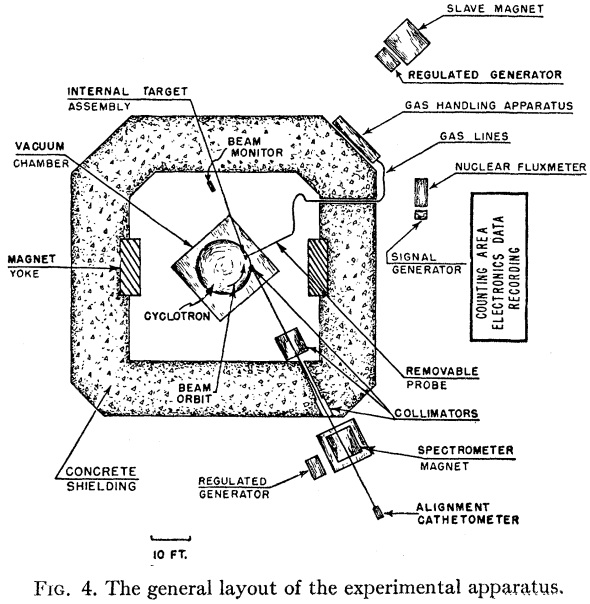

FIG. 4. The general layout of the experimental apparatus.

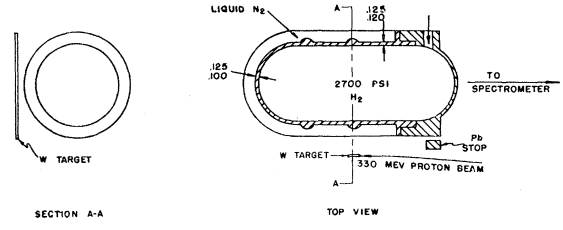

FIG. 5. Internal hydrogen target assembly. The vessel walls are stainless steel.

In order to maintain a reasonable efficiency for the spectrometer—necessary because of the low gamma-ray yields—a larger converter area was used and at the same time the effective height of the detectors was increased. This was done by paralleling Geiger tubes as shown in Fig. 6. The size of the channel width was reduced in the new geometry because of the greater energy dispersion along the "focus line." To further minimize the channel width, an overlap coincidence system was used as follows:

The tubes were spaced so that the edges of adjacent tubes overlapped approximately $\frac{1}{3}$ of a tube diameter as shown in Fig. 7. The detection electronics were arranged so that events in which a particle passed through the overlap portion of the tube could be distinguished from those passing through the central $\frac{1}{3}$ or nonoverlap portion of the tube.

The block diagram of the electronics is shown in Fig. 8. The gating of Geiger-tube outputs by the require-

[10] Chinowsky, Sachs, and Steinberger, Phys. Rev. **93**, 917 (1954).

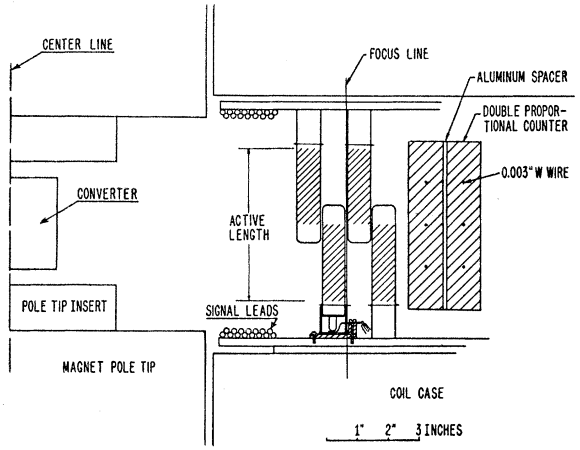

FIG. 6. The side view (cross section) of the tube holder, magnet pole tip, and multiwire proportional counter. The Geiger counters straddle the focus line.

ment of a quadruple coincidence between proportional counters backing up the Geiger-tube banks was used to eliminate accidental background as in the previous spectrometer design of Panofsky *et al.*[9] The Geiger-tube outputs were observed visually with numbered neon lights. The losses which occurred because of rapid flurries of counts (less than 10 percent of total counts) presumably are a random sample of events. The numbering system for the Geiger-tube channels is not easily converted by the observer to the gamma-ray energy so that the observer is in no way prejudiced in which energy events he rejects or misses.

The design of the counter holder and the location of tubes was made from a series of preliminary orbits the accuracy of which was later found to be $\pm 1/10^3$ by the precision orbit analysis (see Section III B).

The background gamma rays we believe are caused by neutral mesons probably produced by scattered protons striking the hydrogen vessel. The background spectrum when corrected by the statistics of the energy channel matrix is shown in Fig. 9. The normalization of the background which is subtracted was chosen so that, in a region well removed from the capture line and the neutral meson gamma-ray flux from hydrogen, the intensity would vanish.

The dependence of these results on the background-subtraction method and variations of efficiency for various energy channels has been considered in detail for the spectrum obtained with deuterium[11] where, because of the relative width and intensities of the spectra, the effect on the energy scale is exaggerated. These effects are negligible in this experiment.

To establish the resolution experimentally, a preliminary measurement of the meson-capture gamma rays was made using several size converters. These spectra, shown in Figs. 10–12, corrected for background, can be analyzed to give a crude mass value and a resolving-power width. Although the statistics are poor, the agreement of the energy scale as obtained with the thin converter (0.010 in.) and the check of the resolution theory is most gratifying. (See Table I.)

The converters were supported on thin slabs of beryllium. The amount of conversion obtained with no tantalum is 10 percent of the total counts as determined with neutral mesons produced at the primary

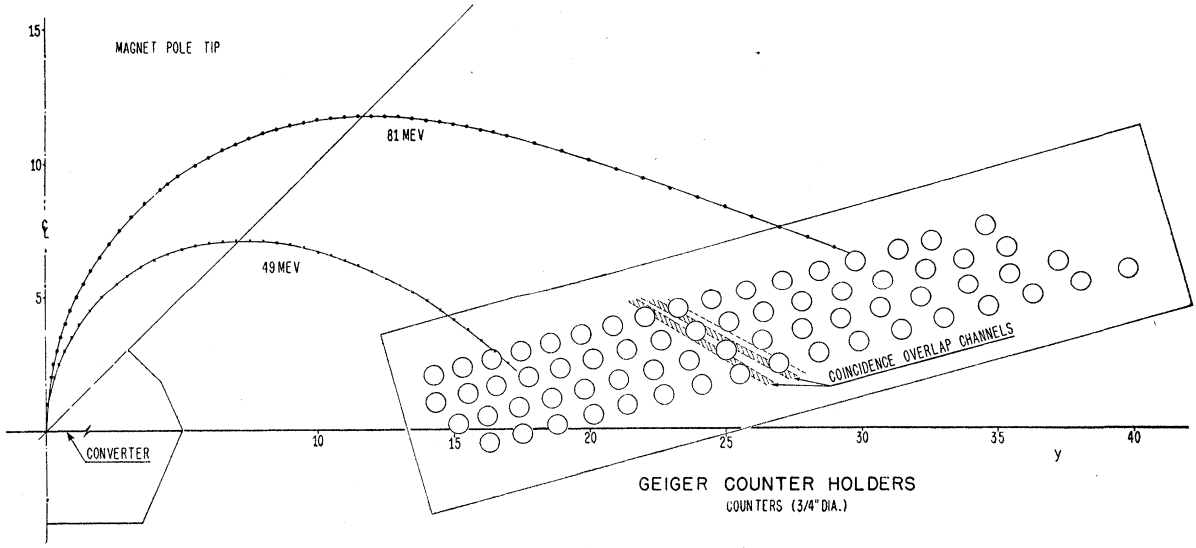

FIG. 7. Top view of counter holder in relation to magnet pole tip. The orbits for 49- and 81-Mev electrons are shown. The overlap channels defined by coincidences between adjacent Geiger tubes are shown for the central energy of the spectrometer. The scale is in inches.

[11] R. H. Phillips and K. M. Crowe, University of California Radiation Laboratory Report No. UCRL-1845 Rev. Following paper [Phys. Rev. **96**, 484 (1954)].

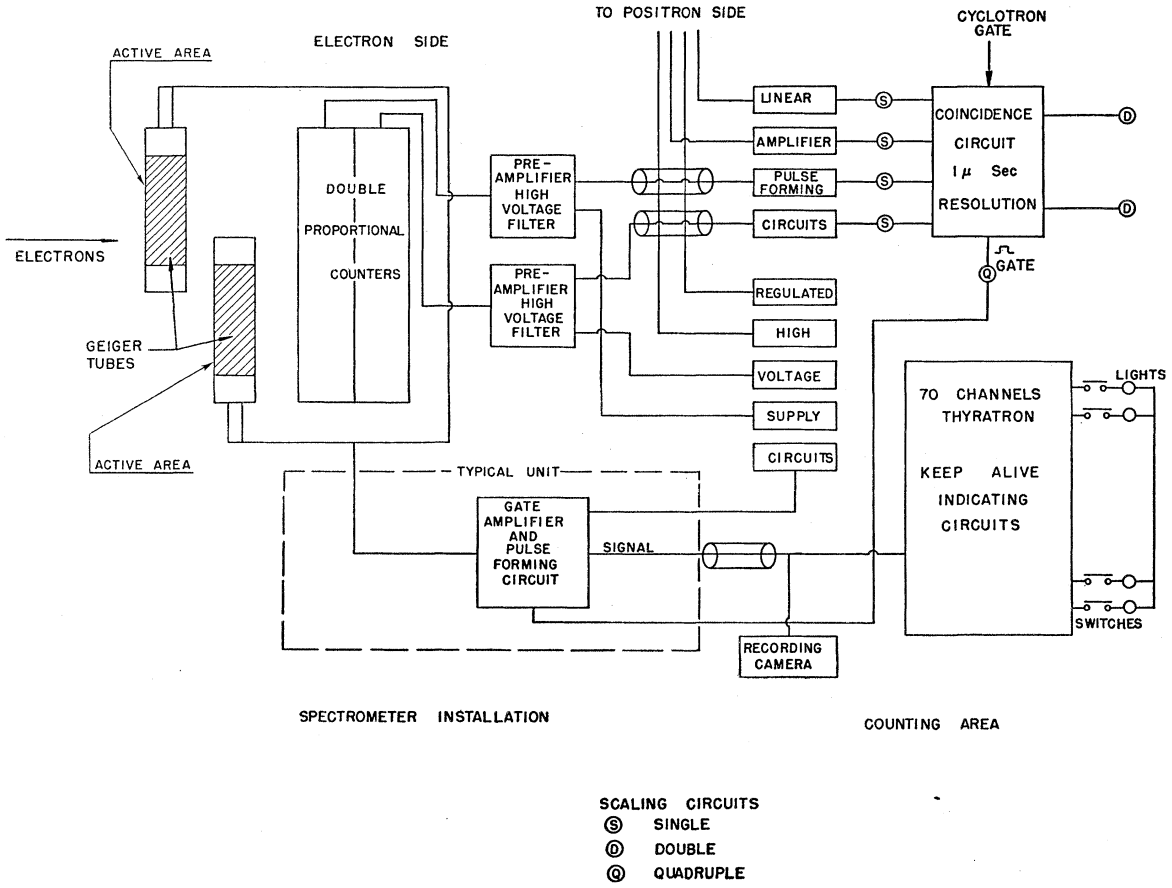

FIG. 8. The electronic block diagram.

target. The no-converter spectrum of the π^0 gamma rays was found to be similar in shape to the converter signal. A short no-converter run was made with only the beryllium holder in place and with the hydrogen vessel filled in order to detect whether any odd effects were being overlooked. Approximately one count per hour was obtained and the few counts were distributed similarly to the converter data, although the data scarcely constituted a spectrum. This run indicated the electronics were not subject to stray counts and cross talk, and that no accidentals occurred that were not caused by pair fragments coming from the converter.

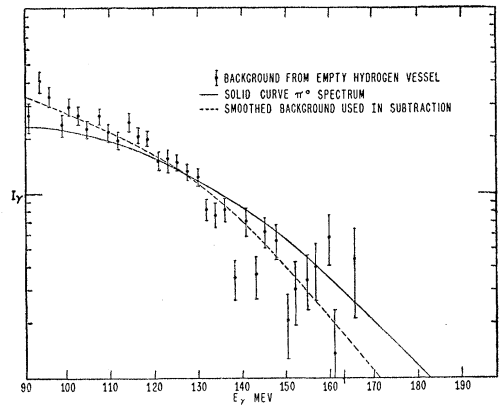

FIG. 9. Gamma-ray background from the empty hydrogen vessel. Probable errors are shown. The solid line is obtained from the π^0 decay gamma's which are produced at the primary target with 340-Mev protons. The dotted line shows the smooth background that was subtracted from the hydrogen data.

There is one other source of concern in the behavior of the spectrometer. This is an apparently reduced efficiency for pair detection by the Geiger tubes. The pair spectrometer in both of the detector layouts records approximately 50 percent of the quadruple events as singles, i.e., only one side of the Geiger-tube array fires. We believe these events arise from a combination of effects:

(a) dead time losses of the Geiger tubes,
(b) measured Geiger-tube end effects which limit the detector vertical window to be less than the proportional counter window,
(c) random variations in the plateau characteristics of the 140-odd Geiger tubes, which were all run at the same voltage, and
(d) accidental gating signals from the proportional counters.

None of these effects is believed to have any influence on the spectrum because of the unique identification of the real events as opposed to the random distribution of the assumed processes. Although the overlap channel efficiency will be affected by a and c, measurements again indicate that the reduction is at most 10 percent. In general the average energy obtained from the data does not depend on the individual tube efficiencies since the counts in any energy channel are averaged over many combinations of energy division of the pair fragments.

III. THEORY OF THE SPECTROMETER

A complete discussion of the determination of the energy scale and the resolving power is not possible here because of space limitations. We shall summarize the major features with special references to those effects which bear on the energy scale. A more detailed account of this subject is to be submitted to the *Review of Scientific Instruments*.[12]

The energy scale of the spectrometer was established in the following manner. The magnetic field was measured in the median plane throughout the regions of interest. A numerical integration of the equations of motion was carried out at three energies of both electron and positron. These orbits began at the center of the converter in the direction of the beam axis. The equations for perturbation of these orbits were solved for various initial conditions, i.e., positions and angles at the converter. Using the known or observed distributions for these initial conditions, the energy distributions were calculated for each type of aberration and these were folded together with the other types of energy aberrations to obtain the resolving power.

TABLE I. Energy values obtained with various converter sizes.

Converter	Theoretical resolution full width at half-maximum	Observed resolving power width	Gamma-ray energy	π^- mass
0.050″ Ta	···	4.5 ±1 Mev	130.0 ±1	274.5 ±2.2
0.020″ Ta	3.3 Mev	3.5 ±1 Mev	129.3 ±0.3	273.0 ±0.6
0.010″ Ta	2.3	2.45 ±0.2	129.19 ±0.12	272.7 ±0.3

A. Magnetic Field

The determination of the absolute magnetic field was made using a nuclear induction fluxmeter in the spectrometer field throughout all the relative field measurements as well as during the cyclotron runs. The uniformity of the magnet was mapped in a mesh which was fine enough so that numerical interpolation methods could be used to find the field for any place in the median plane without increasing the error appreciably above the value at the mesh points.

[12] Kenneth M. Crowe, University of California Radiation Laboratory Report No. UCRL-2050 Rev. I, 1952 (unpublished).

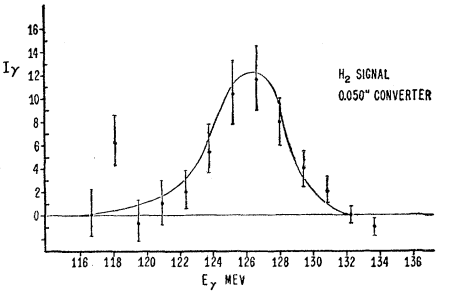

FIG. 10. The pion capture γ-ray spectrum which is obtained by using a 0.050-in. tantalum converter. Probable errors are shown. The solid curve is the estimated resolution. The effects caused by scattering out losses are difficult to include.

The location of the grid was determined by a precision aluminum template. The template was positioned relative to the pole tip insert (indicated in Figs. 6 and 7), which in turn was pinned to the pole tip base.

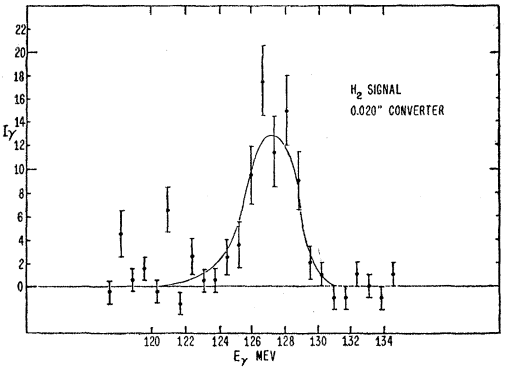

FIG. 11. The capture spectrum obtained by using a 0.020-in. tantalum converter. Probable errors are shown. The solid curve is the calculated resolution.

All positioning of the detectors and converter as well as the main alignment was made relative to this template. The smallest spacing of points was $\frac{1}{2}$ inch in the

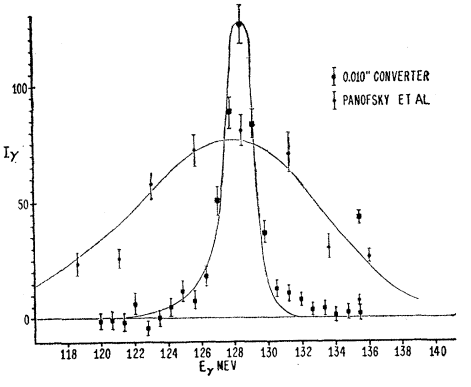

FIG. 12. The capture spectrum measured with the thin target, 0.010-in. tantalum, compared to the spectrum obtained by Panofsky *et al.* The solid curves are theoretical resolution curves. Probable errors are shown.

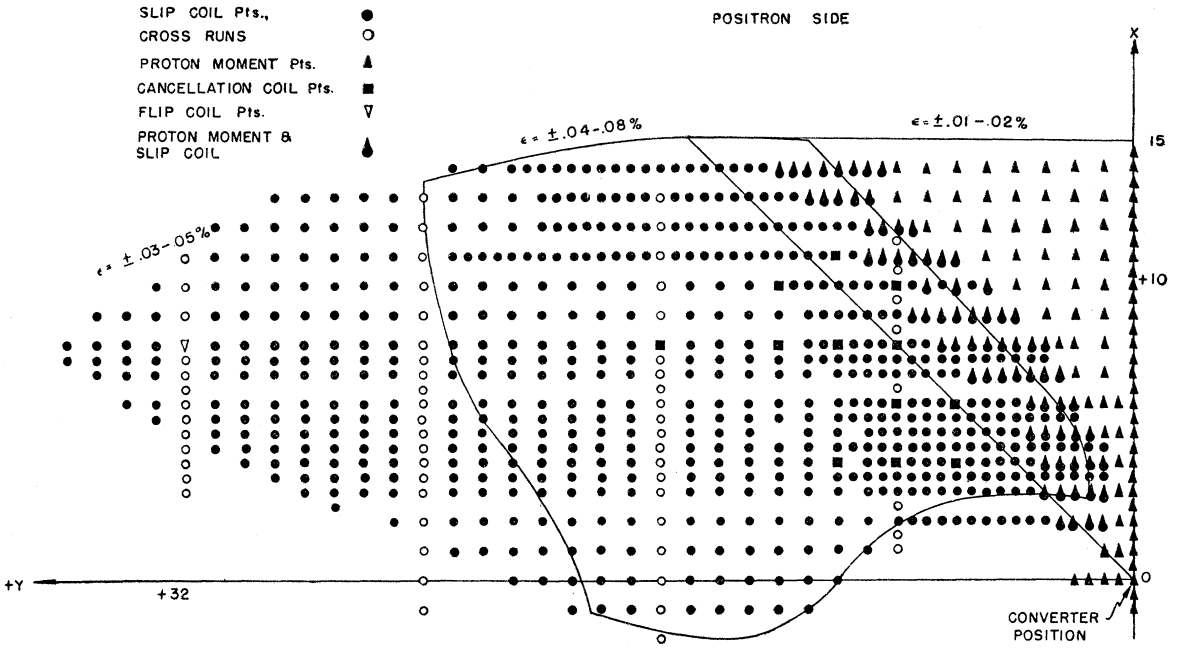

FIG. 13. The grid of field measurements positron side; ϵ's indicate the range of errors in percent of H_0 which are estimated to be associated with each of the regions in the field. The scale is in inches.

regions of rapidly varying field. Figure 13 shows the field grid with the various types measurements.

The bulk of the field measurements (~1000) consisted of relative uniformity runs made with the usual search coil, fluxmeter technique. The slip coil is mounted in a holder such that its electrical center and axis could be adjusted relative to the locating holes in the template. Care was taken to check and eliminate drifts and every measurement was an average of at least three independent measurements.

At a low value of field (~1 percent of the field at the converter), a coil of known area was flipped and the fluxmeter calibrated against a known field. The accuracy of these standards was considerably higher than required.

To eliminate accumulated errors in the long slip-coil runs, a larger grid of ~30 points located in the high-gradient portion of the field was determined by a cancellation method. This was done by rotating two bucking search coils, one in the unknown field and the other in a slave magnet which could be controlled and measured with the proton resonance fluxmeter. The coils were rotated slowly by a geared selsyn system and the difference signal measured with the search coil fluxmeter. These measurements were used in conjunction with the proton resonance data and the data at the low field to calibrate the sensitivity of the slip coil readings, thereby distributing the accumulated errors over short segments of the field.

The errors of the field measurements are summarized in Table II.

TABLE II. Magnetic field errors, expressed as percent of field at pair converter.

A. Errors of each type measurement (standard deviation):	
1. Uniform field data	±0.015%
2. Flip coil data	±0.02 %
3. Cancellation data	±0.03 %
4. Slip coil data	±0.03 %
B. Total error in various regions (standard deviation):	
1. Uniform field	±0.015%
2. High-gradient field	±0.060%
3. Low fields	±0.035%
C. The errors when weighted over these regions averaged over various orbits (probable error)	±0.035%

B. Precise Orbits

The precise energy scale at the detectors was established by computing orbits for particles which were produced at the center of the converter along the beam direction. The numerical method of computation of orbits was chosen keeping the field grid in mind. The radius-of-curvature equation in rectangular coordinates was integrated stepwise. The form of the differential equation for the orbit was

$$\frac{d^2y/dx^2}{[1+(dy/dx)^2]^{\frac{3}{2}}}=\frac{1}{\rho}=\frac{cH(x,y)}{(E^2-(mc^2)^2)^{\frac{1}{2}}}, \tag{10}$$

where dy/dx and d^2y/dx^2 are the first and second derivatives at the orbit in rectangular coordinates, ρ is the radius of curvature, $H(x,y)$ is the magnetic field at (x,y). The field measured at the converter was $H(0,0)=9.12261$ kilogauss, E is the total relativistic

energy and mc^2 the rest energy of the electron or positron; and c is the velocity of light.

The Bessel central difference extrapolation and interpolation formulas were used[13] and the step size ($\sim\frac{1}{2}$ inch to 2 inches) was chosen so that the number of higher differences required for the accuracy necessary was convenient. Six figures were carried throughout the computation. The field values were interpolated from the grid by using four-point Lagrangian interpolation coefficients.[14] An entire orbit averaged 80 steps and seven orbits were carried out (four on one side and three on the other).

The accuracy of the numerical approximations used in the computations was sufficient to give $\sim 1/10^4$ accuracy in the final energy so that the precision of these orbits rested upon the knowledge of the magnetic field. The energy scale along the detector line was fitted to a polynomial to interpolate between calculated orbits. The error introduced because of this procedure was estimated from the relative size of the polynomial coefficients to be $\sim 1/10^4$.

C. Perturbation Orbits

To determine the effect of the large size converter, calculations were made in various approximations for the orbits which deviated from the central or precise orbits. The first approximation to the deviated orbits was obtained by solving the Kerst-Serber vertical and horizontal perturbation equations[15] on the Berkeley differential analyzer.[16]

The equations for the horizontal and vertical motion are

$$\xi_1''+\frac{1-n_1(s)}{\rho^2}\xi_1=0, \tag{11}$$

$$Z_1''+\frac{n_1(s)}{\rho^2}Z_1=0. \tag{12}$$

The definitions of terms which appear in Eqs. (11) and (12) and subsequent equations follow:

ρ, ρ', ρ'' are the radius of curvature and its derivatives along the orbits;
s is the arc length measured along the zero order orbit (primes are derivatives with respect to s);
ξ is the displacement in the horizontal plane normal to the orbit;
Z is the displacement in the vertical plane normal to the orbit;

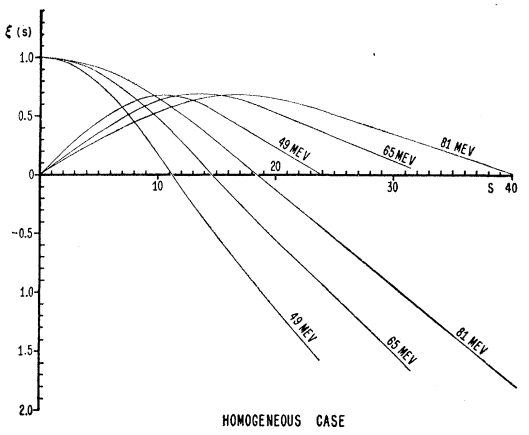

FIG. 14. The family of ξ solutions for the horizontal motion for typical particle energies. For the solutions for which $\xi(s=0)=0$, the initial slope $\xi'(s=0)=\tan\theta_0$. For the other solutions, $\xi'(s=0)=0$ and $\xi(s=0)=1$. s is the arc length measured along the zero order orbit. ξ is the displacement in the horizontal plane normal to the zero order orbit. The scale is in inches and the trajectories end along the focus line.

ξ and Z are small compared to ρ,
$n_1(s)=-(\rho/H)(dH(x,y)/d\eta)$, the first normal derivative of the field, and
η is taken as the outward normal.

In this approximation ξ and Z are uncoupled and satisfy linear second-order differential equations. Thus, for example, the general solution for ξ will be of the form

$$\xi_1(s)=A\xi_A(s)+B\xi_B(s), \tag{13}$$

where ξ_A and ξ_B are the solutions with the initial conditions,

$$\xi_A(s=0)=\xi_0 \quad \text{and} \quad \xi_A'(s=0)=0, \tag{14}$$

and

$$\xi_B(s=0)=0 \quad \text{and} \quad \xi_B'(s=0)=\tan\theta_0, \tag{15}$$

where θ_0 is the initial angle to the beam axis.

Typical solutions for these initial conditions are shown in Fig. 14 for various energy central orbits. From these solutions the first-order focusing against multiple scattering in the horizontal plane can be seen. Also, one can see how the width of the converter is magnified at the detectors. In the 90° apex style spectrometer this width would be in focus along the edge of the tip and this crossover can be seen in the figure. In Fig. 15 we have the corresponding solutions for vertical motion, i.e., perpendicular to the horizontal or medium plane. The strong defocusing action of the fringe field is indicated.

These first-order perturbation results are summarized in Table III A. If one uses these orbits together with the distribution of scattering angles, one can calculate what fraction of the total flux of pair fragments arrives within the vertical window in the detector. This yield will vary for pairs produced at various converter thicknesses. The characteristic scattering parameter is the

[13] J. B. Scarborough, *Numerical Mathematical Analysis* (Johns Hopkins Press, Baltimore, Maryland, 1930); L. J. Comrie, *Interpolation and Allied Tables* (His Majesty's Stationery Office, London, 1936).
[14] *Tables of Lagrangian Interpolation Coefficients* (Columbia University Press, New York, 1944).
[15] D. W. Kerst and R. Serber, Phys. Rev. **60**, 53 (1941).
[16] E. G. Sorenson, University of California Radiation Laboratory Report No. UCRL-1717, 1952 (unpublished); John Killeen, University of California Radiation Laboratory Report No. UCRL-2239, 1953 (unpublished).

TABLE III A. Differential analyzer results. Homogenous solutions of ξ and Z equations $\xi(0)$, $\xi'(0)$, $Z(0)$, $Z'(0)$ are initial conditions $\xi(S_f)$, $\xi'(S_f)$, $Z(S_f)$, $Z'(S_f)$ are terminal values in inches or radians as measured at the focus line.

Negative side initial condition	Final displacement and slope for typical energies 49 Mev	65 Mev	81 Mev
$\xi=0$ $\xi'=\theta_0$	$\xi=0$ $\xi'=-0.0615$	$\xi=-0.026$ $\xi'=-0.0435$	$\xi=+0.0245$ $\xi'=-0.0327$
$\xi=1$ $\xi'=0$	$\xi=-1.630$ $\xi'=-0.127$	$\xi=-1.665$ $\xi'=-0.0992$	$\xi=-1.683$ $\xi'=-0.0840$
$Z=0$ $Z'=\theta_0$	$Z=+3.125$ $Z'=+0.144$	$Z=+3.212$ $Z'=+0.125$	$Z=+3.360$ $Z'=+0.044$
$Z=1$ $Z'=0$	$Z=+1.810$ $Z'=+0.0522$	$Z=+1.860$ $Z'=+0.0486$	$Z=+1.913$ $Z'=+0.0163$
Positive side (check on symmetry of magnet)			
$\xi=0$ $\xi'=\theta_0$		$\xi=+0.024$ $\xi'=-0.0442$	
$\xi=1$ $\xi'=0$		$\xi=-1.651$ $\xi'=-0.0974$	
$Z=0$ $Z'=\theta_0$		$Z=+3.189$ $Z'=+0.1250$	
$Z=1$ $Z'=0$		$Z=+1.795$ $Z'=+0.0458$	

angle at which the distribution has fallen to $1/e$ of the peak value[17]:

$$\theta_m=\left[\frac{4\pi Nz(z+1)e^4}{p^2v^2}\ln\left\{4\pi z^{4/3}Nt\left(\frac{\hbar}{mv}\right)^2\right\}\right]^{\frac{1}{2}}$$
$$\doteq\left(\frac{15}{E}\right)\left(\frac{t}{x_0}\right)^{\frac{1}{2}}. \quad (16)$$

The symbols have the usual meanings: x_0 is the radiation length of the converter material. The value $(21/E)(t/x_0)^{\frac{1}{2}}$ which is commonly used in calculation of this type, is in error owing to plural scattering.[17]

Averaging over energies and converter depths, the calculated yield is obtained as shown in Fig. 16.

The other yield variations which bear indirectly on the aberration corrections are yield *vs* width and yield *vs* height. In the first approximation the yield should be proportional to the area for the same thickness converter. This, of course, assumes that there was a uniform flux of gamma rays over the converter. This last condition was checked visually in the alignment and with 90-Mev neutrons coming from deuterons on the internal target moved in line with the collimating system. A gross check was also made with neutral mesons from this target, although unfortunately the statistics of counts obtained with the various converter sizes were poor. Because of the lack of accuracy of these checks, a small uncertainty has been calculated and included with the final evaluation of errors.

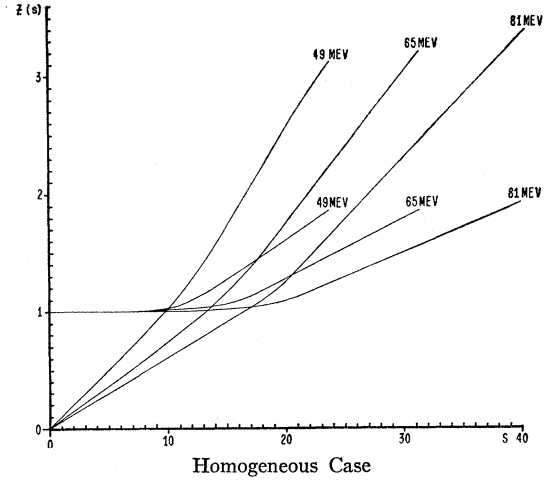

Homogeneous Case

FIG. 15. The family of Z solutions which determines the vertical motion in the first-order theory for typical particle energies. Initial conditions correspond to those in Fig. 14. Z is the displacement in the vertical plane normal to the zero order orbit. The scale is in inches and the trajectories end along the focus line.

It should be noted that effects or yields caused by the second-order perturbations in the Z motion have not been included. The justification for this will become apparent in the following section.

The next approximation calculated was that in which the terms which were neglected in Eqs. (11) and (12) were included as a perturbation to the first-order solution. The form of these terms has been developed by Judd,[18] and the results for motion in the horizontal plane with second-order terms is

$$\xi_2''+\left(\frac{1-n_1}{\rho^2}\right)\xi_2=-\left[\frac{1-2n_1+n_2}{\rho^3}\right]\xi_2^2$$
$$+\left[\frac{-n_1+2n_2+2p'^2-\rho\rho''}{2\rho^3}\right]Z_2^2+\left[\frac{1}{2\rho}\right](\xi_2'^2-Z_2'^2)$$
$$+\left[\frac{\rho'}{\rho^2}\right](\xi_2\xi_2'+Z_2Z_2'). \quad (17)$$

$n_2=(\rho^2/2H)(d^2H/d\eta^2)$, the second normal derivative.

The other symbols are the same as in Eqs. (11) and (12).

The method of solution of this equation was to treat the right-hand side of the equations as a driving term for the first-order equation substituting in the right-hand side the first-order solutions corresponding to the particular kind of orbit perturbation being solved. The

[17] B. Rossi and K. Greisen, Revs. Modern Phys. **13**, 240 (1941); J. Ashkin and H. A. Bethe in *Experimental Nuclear Physics*, edited by E. Segrè (John Wiley and Sons, Inc., New York, 1953), Vol. I, Part 2; Hansen, Lanzl, Lyman, and Scott, Phys. Rev. **84**, 634 (1951).

[18] David Judd (private communication).

equations thus became

$$\xi_2''+A(s)\xi_2=R(s,\xi_1(s),Z_1(s),\cdots). \quad (18)$$

The first-order solution can be subtracted off since it satisfies Eq. (18) with $R=0$. Thus we obtain the second-order displacement at the final value of s, i.e., the detector position for various combinations of ξ_1 and Z_1 where these in turn are the result of the initial conditions set by Eqs. (14) and (15).

Let us take for example the second-order perturbation in ξ for motion in the Z direction. Figure 17 shows the result obtained for $R(s)$ with the initial conditions $Z_1(0)=1$, $Z_1'(0)=0$, for three energies. Figure 18 shows the solution for $\xi_2(s)$. Notice that the perturbations begin at zero ($\xi=0$ and $\xi'=0$) corresponding to the assumed initial conditions and the final value is obtained by following the solution to the intersection of the central orbit with the detector line. With this solution one can calculate the apparent energy shift which results from the complicated behavior in the fringing field off the median plane of the particle which has started at the converter 1 inch above the center.

TABLE III B. Second-order results. The cases correspond to the solution of the ξ equation with higher-order terms as explained in text.[a] Final displacement is in inches at the focus line.

	Initial conditions				Final displacement		
Case	ξ	ξ'	Z	Z'	$\xi(S_f)49$	$\xi(S_f)65$	$\xi(S_f)81$
1	1	0	0	0	−0.0011	−0.0039	+0.0013
2	0	θ_0	0	0	−0.0786	−0.0496	−0.0259
3	1	θ_0	0	0	−0.0734	−0.0447	−0.016
4	−1	θ_0	0	0	−0.0689	−0.0545	−0.033
5	0	0	1	0	−0.1293	−0.1232	−0.0837
6	0	0	0	θ_0	−0.3355	−0.2369	−0.2125
7	0	0	1	θ_0	−0.8117	−0.6235	−0.5040
8	0	0	−1	θ_0	−0.1244	−0.0835	−0.0792
9	0	0	1	$\theta_0/2$	−0.3939	−0.2515	−0.2496
10	0	0	−1	$\theta_0/2$	−0.0463	−0.0396	−0.0364
11	1	θ_0	1	θ_0	−0.7122	−0.6570	−0.556
12	−1	θ_0	1	θ_0	−0.7058	−0.6915	−0.580
13	1	θ_0	−1	θ_0	−0.1300	−0.1300	−0.158
14	−1	θ_0	−1	θ_0	−0.1646	−0.1383	−0.086

[a] Kinetic energy 49 Mev 65 Mev 81 Mev
$\theta_0=$ 0.100 0.0750 0.0600

This procedure is carried out for each initial condition and the various combinations, to explore mixing of the various effects. The results of these calculations are shown in Table III B.

The same kind of procedure can be followed with the Z motion in second order. The vertical equation is

$$Z_2''+(n_1/\rho_2)Z_2=[(-2n_1+2n_2)/\rho^3]\xi_2Z_2 +[1/\rho](\xi_2'Z_2')+[\rho'/\rho^2](\xi_2'Z_2-Z_2'\xi_2). \quad (19)$$

By inspection, one can see that in the method used in solving the equation there is a simplification in the extent of these perturbations. For cases where either $Z_1(s)$ and $Z'(s)$ or $\xi_1(s)$ and $\xi_1'(s)$ vanish, the driving term also vanishes. Therefore the Z solutions consist entirely of mixing terms. The maximum size of Z_2 is of the same order as the other second-order perturbations so that the first-order theory for detector window is in error by a small amount. The Z solutions thus effect the energy scale only by introducing a small change in the distribution for orbits which have both large Z and ξ displacements. This correction has been estimated and it has been included among sources of error for the second-order energy correction.

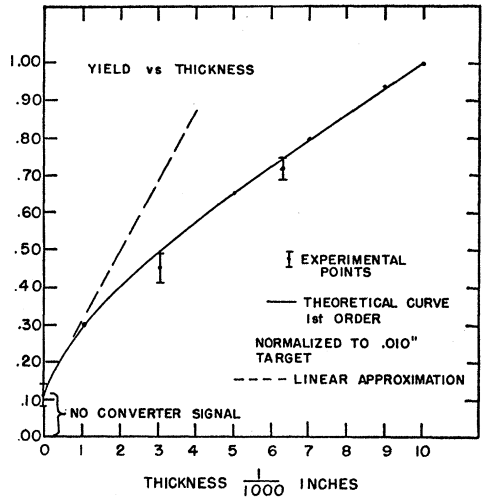

FIG. 16. The theoretical and experimental yields for various converter thicknesses. The theoretical curve has been used to weight all the effects in the resolution which depend upon converter thickness. The experimental points were measured with neutral meson γ rays; probable errors are shown.

Finally, the accuracy of these perturbation solutions is estimated both from the reproducibility of the differential analyzer results and the accuracy of the field gradients which come into the calculations, to be approximately 1 to 5 percent of the final displacement, depending on the initial conditions. The errors introduced in the neglect of the higher terms in the perturbation calculation as well as that introduced by neglect of still higher terms in the differential equations were checked in the important cases and the effects were found to be well within the accuracy of the perturbation solutions.

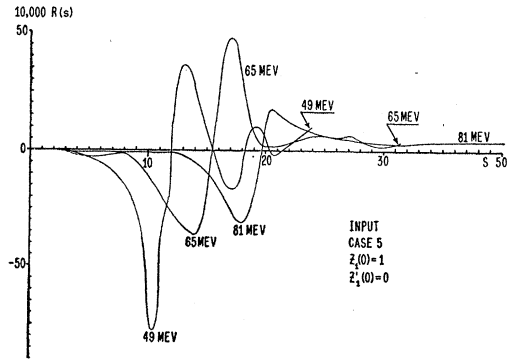

FIG. 17. The analyzer input function for the initial displacement in the vertical direction $Z(0)=1$, $Z'(0)=0$; Case 5. The scale is in inches and the trajectories end along the focus line.

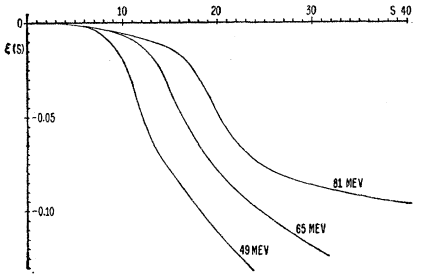

FIG. 18. The solution in the median or ξ plane for the vertical height effect of the converter. Case 5. The scale is in inches and the trajectories end along the focus line.

D. Resolving Power

The major resolving power components will be considered in the order in which they were folded together rather than in the order of their relative importance. In evaluating the energy of the gamma ray, the relevant quantity is the average shift (the first moment) of the resolving power which can be shown[12] to be the algebraic sum of the shifts of the components. In Table IV the energy shifts for each effect are shown for comparison.

Pairs that are produced in the converter lose energy traversing the converter by both ionization and radiation. The theory of these processes is discussed thoroughly by Ashkin and Bethe.[17]

In computing the resolving width caused by variation in the energy loss we have included the following effects:

1. A Landau type distribution[19] for the fluctuations of ionization loss.

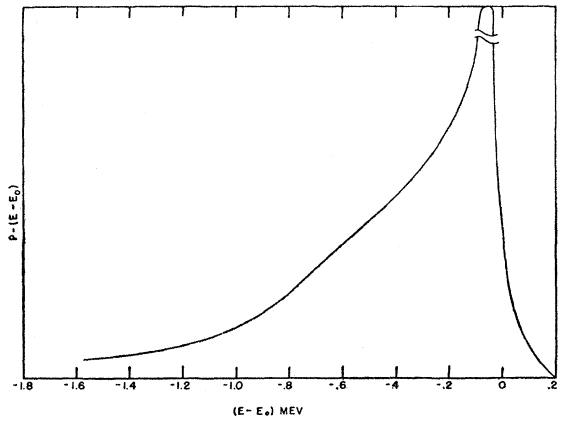

FIG. 19. The resolution caused by first-order converter thickness effects: ionization energy loss, radiation energy loss, and horizontal scattering, averaged over the converter.

[19] L. Landau, J. Phys. U.S.S.R. **8**, 201 (1944); K. R. Symon, Harvard University, thesis, 1948 (unpublished); A. Bohr, Kgl. Danske Videnskab. Selskab, Mat.-fys. Medd. **24**, No. 19 (1948); T. Bower and F. X. Roser, Phys. Rev. **83**, 689 (1941); F. X. Roser and T. Bower, Phys. Rev. **82**, 284 (1951); **85**, 992 (1952); R. Hofstader and A. Hudson, Phys. Rev. **88**, 589 (1952); W. L. Wittemore and J. C. Street, Phys. Rev. **76**, 1786 (1949); Goldwasser, Mills, and Hansen, Phys. Rev. **88**, 1137 (1952); Igo, Clark, and Eisberg, Phys. Rev. **89**, 879 (1953).

2. Sternheimer's correction[20] because of the density effect for ionization loss in the converter.

3. The mean ionization potential for the converter (tantalum) interpolated from Bakker and Segrè.[21]

4. The correction in the bremsstrahlung[22] cross section as indicated from recent experiments ($\sim$7.5 percent in tantalum).

5. The moments of the distribution were computed by cutting off the tails of the radiation straggling curves at 6 Mev and including the reduction in detection efficiency along with the purely geometrical effects for each converter thickness. This cutoff procedure was used in calculating the first moment of the data to eliminate the dependence of the moment on the assumed cutoff. The same procedure was then repeated by cutting off at 12 Mev and the results agreed within the statistical error.

These distributions were then combined with the scattering in the horizontal plane which was deduced from the perturbation orbit calculations. The shape of this distribution is based on the Gaussian angular distribution for multiple scattering. The errors in the assumed distribution are not consequential. In fact, due to a fortuitous cancellation of several opposing effects, the net moment of the resolution was found to be almost independent of the assumed mean-square scattering angle.

TABLE IV. Shifts in the energy scale.

1. Ionization loss	
Converter	−0.509 Mev
Air	−0.174 Mev
2. Radiation (cut off at 6 Mev)	−0.411 Mev
3. Horizontal scattering	
First-order theory	+0.003 Mev
Second-order perturbation	−0.100 Mev
4. Converter horizontal width	
First-order theory	+0.709 Mev
Second-order perturbation	−0.002 Mev
5. Converter vertical height and scattering	
Second-order theory	−0.310 Mev
6. Detector channel location	
(tube positions and central orbits)	−0.146 Mev
Net moment −0.940 Mev	

The resolutions for these effects were averaged together over the converter thickness and the resulting curve is shown in Fig. 19.

The channel width was calculated knowing the precise central energy scale and the accurate counter locations. In the positioning (made before the precise

[20] W. F. G. Swann, J. Franklin Inst. **226**, 598 (1938); E. Fermi, Phys. Rev. **56**, 1242 (1939); **57**, 485 (1940); G. C. Wick, Nuovo cimento **1**, 302 (1943); Ricerca sci. **11**, 273 (1940); O. Halpern and H. Hall, Phys. Rev. **57**, 459 (1940), Phys. Rev. **73**, 477 (1948); R. M. Sternheimer, Phys. Rev. **88**, 851 (1952).

[21] R. L. Mather and E. Segrè, Phys. Rev. **84**, 191 (1951); C. J. Bakker and E. Segrè, Phys. Rev. **81**, 489 (1951).

[22] C. R. Emigh, Phys. Rev. **86**, 1028 (1952); DeWire, Ashkin, and Beach, Phys. Rev. **82**, 447 (1951); Phys. Rev. **83**, 233, 476, 505 (1951); J. L. Lawson, Phys. Rev. **75**, 433 (1949); C. D. Curtis, Phys. Rev. **81**, 308 (1951); C. D. Curtis, Phys. Rev. **89**, 123 (1953).

orbits were completed) an uncertainty was present in the approximate energy scale which was later accurately determined. The resolution width which resulted from this uncertainty is shown in Fig. 20. This resolution was folded in with the previous result.

The distribution because of the width of the converter was computed assuming uniform flux and equal detection efficiency. The main effect here is obtained from the first-order calculations for the orbits which are produced in the strip of converter in the horizontal plane which leave normally to the converter. One can show that the displacement at the detector $\delta\xi(s_f)$, can be approximated by the expression

$$\delta\xi(s_f)\cong\xi_1(s_f)\xi_1'(s_f)/\tan\phi, \tag{20}$$

where s_f refers to the final value for the arc length ξ_1, ξ_1' the first order solution and its derivative, and ϕ is the angle of intersection between the counter line and the central unperturbed orbit.

Since $\xi_1(s_f)$ and $\xi_1'(s_f)$ are both proportional to the initial conditions $\xi(s=0)$, one obtains that the energy

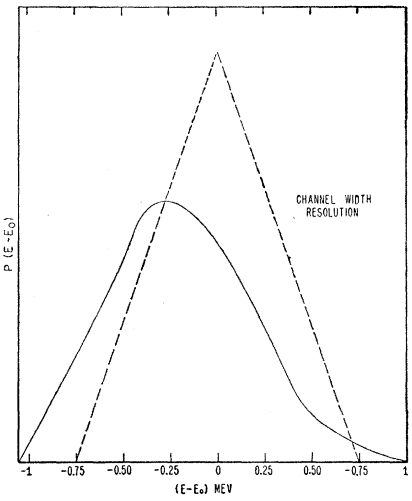

FIG. 20. The finite detector channel width resolution. The dotted curve is the ideal resolution for a single pair of counters located at positions such that $E^+ + E^- = E_0$. The solid curve is the actual resolution when averaged over slight errors in location and in channel widths.

shift is given by

$$\Delta E \propto \xi(0)^2. \tag{21}$$

The distribution can be found to be

$$P(\Delta S) \propto (\Delta E)^{-\frac{1}{2}}. \tag{22}$$

One must average properly over the division of the pairs and the result is shown in Fig. 21.

The second-order effect of multiple scattering in the horizontal plane can be calculated in a manner similar to the horizontal width calculations.

The last major effect results from the vertical motion. These calculations were complex since in obtaining

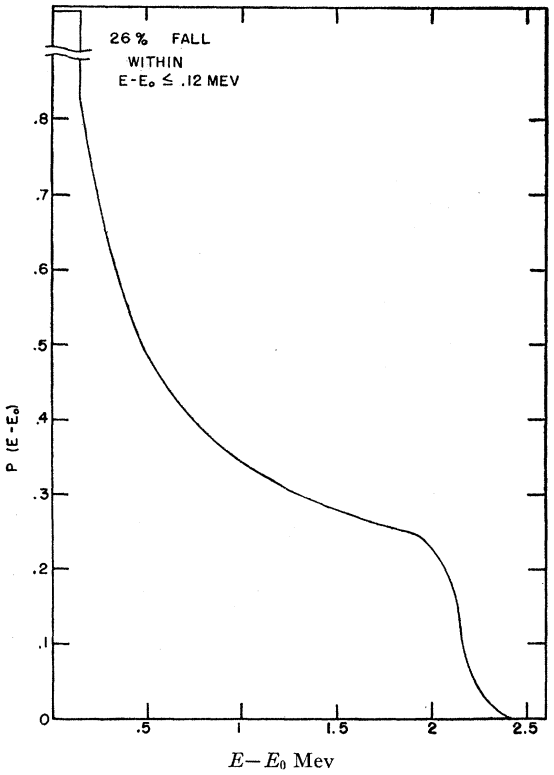

FIG. 21. Resolving power resulting from the finite lateral width of the converter. This depends only upon the first-order solutions to the orbit perturbation problem. (The small effects of the second-order orbit perturbation theory have not been included in this curve.)

the distribution of initial conditions, the motion resulting from vertical displacement and vertical scattering is not at all separable either in the manner in which the perturbation effects occur or in the way the initial conditions are restricted by the counter acceptance windows. The calculation, although lengthy, followed closely the method outlined in the previous calculations. The resulting distribution is shown in Fig. 22. Fortunately for the accuracy required, the detailed analysis was necessary only to assure that there were no larger nonlinear effects present which may have resulted from the complexity of the motion. In fact, none were large and the resulting moment is not sensitive to the complex features of the calculations. The final fold of the resolution is shown in connection with the data in Fig. 23. The vertical normalization is arbitrary. The energy scale is labeled to correspond to the channels in which the data were recorded.

IV. EXPERIMENTAL RESULTS

To arrive at the value for the gamma-ray energy, the first moment of the data was obtained. The resolution has a net moment as determined algebraically in Table III. In addition the zero of the resolution appears on the folded curve and this is indicated by the arrow

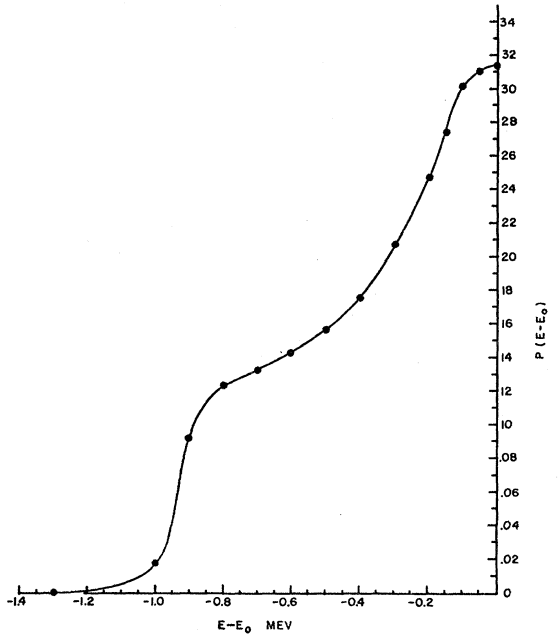

FIG. 22. The second-order energy resolution component caused by vertical scattering and vertical height of the converter; Case 4, 5.

just to the right of 129 Mev on the energy scale of Fig. 23. The value for the energy which results from a visual fit of the resolution to the data agrees well with the value obtained by the moments. We obtain for the gamma-ray energy:

$$E_\gamma = 129.19 \pm 0.12 \text{ Mev}. \tag{23}$$

The relation between the pion mass and the gamma-ray energy is given as follows:

$$E_\gamma = M_\pi c^2 - \frac{E_\gamma^2}{2M_n c^2} + \frac{1}{8}\frac{E_\gamma^4}{(M_n c^2)^3} - (M_n - M_p)c^2 - \left(\frac{\alpha^2}{2}\right) M_\pi c^2 + \cdots. \tag{24}$$

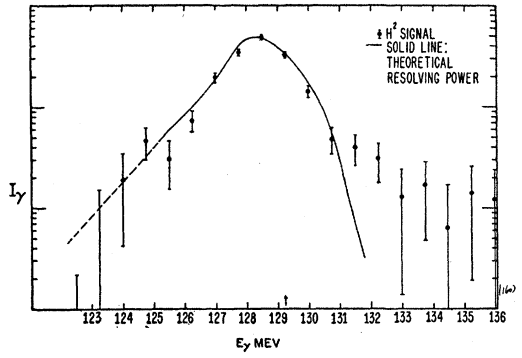

FIG. 23. The resolution curve which includes all the first and second-order effects calculated by folding together the resolution components. The data is shown with probable errors.

The terms in order of importance are the meson rest mass, the recoil energy of the neutron, the neutron-proton mass difference, and the Bohr K-shell energy. In calculating the meson mass we have used the electronic rest mass from DuMond and Cohen,[23] and the neutron-proton mass difference from Robson's work[24]:

$$(M_n - M_p)c^2 = 1.293 \pm 0.013 \text{ Mev}. \tag{25}$$

In calculating the radius of curvature (Eq. 10), the absolute field was measured using the magnetic moment as obtained by Thomas, Driscoll, and Hipple.[25]

The errors have already been discussed in some detail and they appear in summary in Table V.

In evaluating the statistical error (G), we can fit the data with a gaussian of root-mean-square width of 1.0 Mev. This fit is satisfactory if one ignores all points which are three or more standard deviations from the mean. Making the usual analysis based on the total number of events, we arrive at a probable error of ±0.048 Mev.

TABLE V. Summary of errors in mass measurement.

A	Field errors: (probable error from Table II)	$\pm 3.5/10^4$
B	Field fluctuations during cyclotron run: ($\frac{1}{2}$-maximum deviation)	$\pm 1.0/10^4$
C	Geometry errors, templates, counters, leveling, etc:	$\pm 3.5/10^4$
D	Central orbit calculations:	$\pm 1.0/10^4$
E	Probable error in ionization and radiation loss due to uncertainties in the measured corrections to the theory:	$\pm 2/10^4$
F	Errors in computations of perturbation orbits: (see Table III):	$\pm 3/10^4$
G	Statistical error:	±0.048 Mev
	or	$\pm 3.7/10^4$
H	Total error obtained from known sources:	±0.095 Mev
	or	$\pm 0.21\ m_e$
I	Additional error (see below):	$\pm 6/10^4$
J	Total error assigned by experimentors:	$\pm 0.27\ m_e$

In addition to the usual sources of error we have included an additional estimate of errors (I) which fall into two classes.

(1) There are a number of small sources of error which were calculated to be negligible which it was not possible to investigate with sufficient accuracy because of the low counting rates. Although the theory indicates these effects to be unimportant (that is, less than $1/10^4$) these may contribute in a systematic rather than random manner.

(2) We also are including here the contribution which represents an estimate of uncertainties of the error estimates. For example, there are uncertainties in the

[23] J. W. M. DuMond and E. R. Cohen, Am. Scientist **40**, 447 (1952).

[24] J. Robson, Phys. Rev. **83**, 349 (1951); Hornyak, Lauritsen, Morrison, and Fowler, Revs. Modern Phys. **22**, 291 (1950).

[25] Thomas, Driscoll, and Hipple, Phys. Rev. **75**, 902 (1949); Phys. Rev. **78**, 787 (1950); N. F. Ramsey, Phys. Rev. **77**, 567 (1950); H. A. Thomas, Phys. Rev. **80**, 901 (1950).

background normalization, the yield runs, vertical scattering losses in higher order, etc.

Our result is

$$M_{\pi^-}=272.74\pm0.27\ m_e. \tag{26}$$

The π^0 mass which is derived from Eq. (9) is

$$M_{\pi^0}=263.9\pm0.7\ m_e. \tag{27}$$

The μ^+ mass is derived from Eq. (4) to be

$$M_{\mu^+}=206.33\pm0.28\ m_e. \tag{28}$$

The last value assumes the π^+ and π^- to have the same mass.

V. ACKNOWLEDGMENTS

The authors take pleasure in acknowledging the assistance so generously offered by members of the Radiation Laboratory Staff. Professor W. K. H. Panofsky, now at Stanford University, has guided the entire program.

The Magnetic Measurements Group, under Mr. Duane Sewell, contributed over a thousand field measurements. Mr. Robert Teeters set up the field measurements and made the preliminary field calculations from which the spectrometer design was made. The lengthy reduction of the precise field measurements was made by Mr. Harold B. Knowles and Mr. Glen Lambertson. The calculations of the orbits were made by Mrs. Ardith Kenney and others under the direction of Mr. John Killeen of the Computing Section of the Theoretical Group. Dr. Louis Henrich and Dr. David Judd suggested the method of approach that was used in these calculations. The design and construction of the equipment represents the joint effort of most of the shops of the Laboratory. The cyclotron crew, under Mr. James Vale, provided the bombardments which lasted over a week. The real credit for the success of the experiment, however, belongs to the people who did many hours of tedious work, accurately and skillfully, within the groups named above.